The interplay of rifting, magmatism and formation of geothermal resources in the Ethiopian Rift constrained by 3-D magnetotelluric imaging

M.L.T. Dambly[1], F. Samrock[1], A. V. Grayver[2,3], M. O. Saar[1,4]

[1]Geothermal Energy and Geofluids group, Institute of Geophysics, Department of Earth Sciences, ETH Zurich, Sonneggstrasse 5, 8092 Zurich, Switzerland

[2]Institute of Geophysics and Meteorology, University of Cologne, Albertus-Magnus-Platz, 50923 Cologne, Germany

[3]Earth and Planetary Magnetism group, Institute of Geophysics, Department of Earth Sciences, ETH Zurich, Sonneggstrasse 5, 8092 Zurich, Switzerland

[4]Department of Earth and Environmental Sciences, University of Minnesota, 55455 Minneapolis, USA

Key Points:

- First 3-D multi-scale magnetotelluric model images the entire transcrustal tectono-magmatic system below the Main Ethiopian Rift.
- A lower crustal magma ponding zone feeds a fault controlled magmatic mush system providing heat for the geothermal system of Aluto volcano.
- Eastern and western volcano-tectonic lineaments share a common lower crustal magma source with an estimated melt fraction of 7 percent.

Corresponding author: Marie Luise Texas Dambly, `mdambly@ethz.ch`

Abstract

The Main Ethiopian Rift is accompanied by extensive volcanism and the formation of geothermal systems, both having direct impact on lives of millions of local inhabitants. Although previous studies from the region found evidence that asthenospheric upwelling and associated decompression melting provide melt to magmatic mush systems that feed the tectono-volcanic segments in the rift valley, no geophysical model imaged these regional and local scale transcrustal structures within a single comprehensive 3-D model. To fill this gap, we combined regional and local magnetotelluric data sets to obtain the first multi-scale 3-D electrical conductivity model of the central Main Ethiopian Rift. The model clearly images a magma ponding zone with up to 7 vol. % melt at the base of the crust ($30 - 35$ km b.s.l.) in the western part of the rift, its connection to Aluto volcano via a tectonically controlled transcrustal magmatic mush system and how the melt, stored at shallow crustal depths (≥ 4 km b.s.l.), supplies heat for Aluto's geothermal system. Our model provides evidence that different volcano-tectonic lineaments in the rift valley share a common melt source, which has been debated in the past. The presented multi-scale model provides new constraints as well as geologic insights into the melt distribution below the rift and will facilitate future geothermal developments and volcanic hazard assessments in the Main Ethiopian Rift.

Plain Language Summary

Continental rifting is a fundamental process of plate tectonics that breaks continents apart to ultimately form new oceans. The landscape of the Main Ethiopian Rift (MER) is characterized by abundant volcanism and hot springs, which indicate presence of geothermal resources formed by magmatic heating of subsurface water. In our study we present a 3-D subsurface image of the magmatic system and geothermal reservoir beneath Aluto volcano in the MER. The model shows the electrical conductivity distribution of the subsurface which allows us to infer the distribution of electrically conductive melt. This is the first model that provides a high-resolution image of the entire magmatic system below the MER from the deep magmatic melt source up to the surface. The new model images for the first time how geothermal reservoirs form as a consequence of rifting related volcanic activity thereby providing a clear illustration of fundamental geological processes. These results also have a high societal relevance by providing a basis for volcanic risk assessment and contributing to a better understanding of how the sustainable green geothermal energy resources form.

1 Introduction

The East African Rift system (EARS) is a prominent continental rift that shaped the landscape of East Africa, including the East African Plateau, rift valleys and numerous volcanoes. Rifting and rift-related volcanism in East Africa played a role in early human evolution (King & Bailey, 2006) and to this date affect the life of humans due to volcanic hazards (Biggs et al., 2021), but also by providing rift-associated natural resources (Benti et al., 2023; Burnside et al., 2021). A large number of studies, especially in the northern part of the EARS, which includes the Main Ethiopian Rift (MER), have provided a wealth of information and knowledge on the geodynamic processes that initiated and drive rifting and associated volcanism in the EARS (e.g. Agostini et al., 2011a; Casey et al., 2006; Corti, 2009; Ebinger, 2005; Kendall et al., 2005; Kendall & Lithgow-Bertelloni, 2016; Keranen & Klemperer, 2008, and references therein).

One of the main findings of these studies is that neither mechanical stretching nor magmatic upwelling could be the the major driver of rifting alone, but it is a rather complex interplay between these processes (e.g. Beutel et al., 2010; Buck, 2004; Kendall et al., 2005). Active magmatism and volcanism in the MER is sustained by asthenospheric upwelling (e.g. Gallacher et al., 2016; Rychert et al., 2012). The main hypothesis is that decompression melting occurs in the upper mantle, melt intrudes into the lithosphere, where it feeds magmatic dykes and sills leading to the formation of volcanic systems in the MER (Chambers et al., 2022; Gallacher et al., 2016; Kendall et al., 2005). Petrological studies and geological mapping (e.g. Hunt et al., 2020; Mazzarini et al., 2016; Rooney et al., 2011) from the central part of the MER (CMER) observed a correlation between the monogenetic vent distribution and fault systems (Fig. 1), which implies that a tectono-magmatic interplay drives the rifting. Multiple studies proposed that a complex magmatic system with magma stalling and fractionating at multiple depths within the crust exists below the western Silti Debre Zeyit Fault Zone (SDFZ) (Iddon & Edmonds, 2020; Mazzarini et al., 2013; Rooney et al., 2011). The SDFZ displays only minor surface expression of faulting (Agostini et al., 2011a) and is a largely aseismic area within the study region (Keir et al., 2006). In contrast, the eastern Wonji Fault Belt (WFB) has been observed to be seismically more active than the SDFZ (Seismic data from 2001-2003 presented in Keir et al., 2006, Fig.4), hosting present-day crustal extension with well-developed magmatic pathways (Corti et al., 2020; Mazzarini et al., 2016, 2013; Rooney et al., 2011). Magma rises quickly under the WFB and fractionates at low pressures corresponding to about 5 km depth (Gleeson et al., 2017;

Iddon & Edmonds, 2020; Rooney et al., 2011). Along the WFB, long-lived silicic peralkaline volcanoes are found with shallow magma chambers that have undergone several phases of eruption and recharge (Fontijn et al., 2018). Active magmatism and extensional strain along the WFB created ideal geological conditions for the formation of high-temperature geothermal resources (e.g. Jolie et al., 2021).

However, there is still a lack of geophysical subsurface models for the MER that would constrain the 3-D distribution of melt and image magmatic pathways across the continental crust. Such geophysical subsurface images are critical for understanding controls on magma transport, magma emplacement under rift-aligned segments and the formation of numerous magma-driven geothermal systems in the MER (e.g. Benti et al., 2023; Jolie et al., 2021). The exploitation of these geothermal resources would be beneficial for the local society (IRENA, 2020). As a source of clean and renewable baseload energy, these geothermal resources can satisfy the growing energy demand and sustain the local economic growth. Numerous countries along the EARS plan to expand exploitation of renewable geothermal energy resources (IRENA, 2020). Ethiopia is currently aiming at installing 1000 MWe of its estimated 10.000 MWe geothermal energy potential (Benti et al., 2023; Burnside et al., 2021).

Our study focuses on the area of Ethiopia's only producing geothermal power plant, Aluto-Langano. The power plant is in operation since 1998 and has an installed capacity of 7.3 MWe (Benti et al., 2023). Expansion work to reach 75 MWe is underway, with four new wells having been drilled in 2022 (capitalethiopia.com, 2022). Our primary goal here is to investigate the magmatic heat source of Aluto's geothermal system and how it is connected to a deeper lower crustal magmatic system. To this end, we will use the magnetotelluric (MT) method and image the 3-D electrical conductivity structure of the subsurface.

Previous MT and seismic studies from this region have identified electrical conductivity and shear wave velocity anomalies in the lower crust under the SDFZ (Hübert et al., 2018; Kim et al., 2012; Samrock et al., 2015). The lower crustal seismic anomalies have been interpreted as a lithospheric melt ponding zone. However, the lateral extent of this anomaly and potential links to Aluto's magmatic reservoir under the WFB remain poorly constrained. Further, it remains unclear whether volcanoes along the WFB and the SDFZ are related to a common melt ponding zone or whether their magmas originate from separated parental melt sources as suggested by e.g. Fig. 8 in Rooney et al. (2011).

To address these questions and better constrain the structure below Aluto, we analyzed a new MT dataset that covers both the rift and the Aluto volcanic complex. Our goal is to obtain a new multi-scale 3-D electrical conductivity model of this area in the CMER (Fig. 1) and resolve both regional-scale structures in the lower crust and local structures related to Aluto's upper crustal magmatic and geothermal reservoirs.

2 Method and Data

To image the melt distribution across the rift and constrain the structures of Aluto's magmatic and geothermal reservoirs, we obtain the subsurface 3-D electrical conductivity distribution employing the (passive) magnetotelluric (MT) method (Berdichevsky & Dmitriev, 2008; Chave & Jones, 2012). Broadband MT responses are sensitive to electrical conductivity structures across a wide range of length scales, providing a unique opportunity to study the subsurface from the near surface and through the crust and upper mantle. More details on the MT method are provided in the Supplementary Information (SI) (SI: Text S1).

2.1 Data

We combine data from regional and local MT surveys in the CMER, as is shown in Fig. 1. The regional dataset, collected within the RiftVolc Project (Hübert & Whaler, 2020), consists of 33 MT stations that are distributed across the rift over a distance of 120 km with average site spacings between 4 km and 13 km (SI: Tab. S1). These regional-scale MT survey was supplemented by a local dataset of ETH Zurich and the Geological Survey of Ethiopia (GSE) (Samrock et al., 2010), consisting of 165 sites that cover the edifice of the Aluto volcano (15 × 15 km), with an average site spacing of 0.7 km. The MT transfer functions cover a period range of $T = 10^{-2} - 10^{3}\,\mathrm{s}$. For this period range and for the averaged electrical conductivity distribution in the study area, the penetration depth is calculated to range between 0.5 and 92.5 km, thereby providing a sufficient range for imaging both near-surface and crustal structures (SI: Fig. S2).

Maps of phase tensor data displayed as ellipses at MT stations for representative periods convey a first impression of the subsurface conductivity structure (Fig. 2). In general, phase tensor ellipses can reveal (i) lateral conductivity contrasts by increased ellipticities, (ii) the strike of lateral conductivity contrasts by the direction of their principal axis (with a 90° ambiguity), (iii) increasing conductivities with depth in case their maximum phase

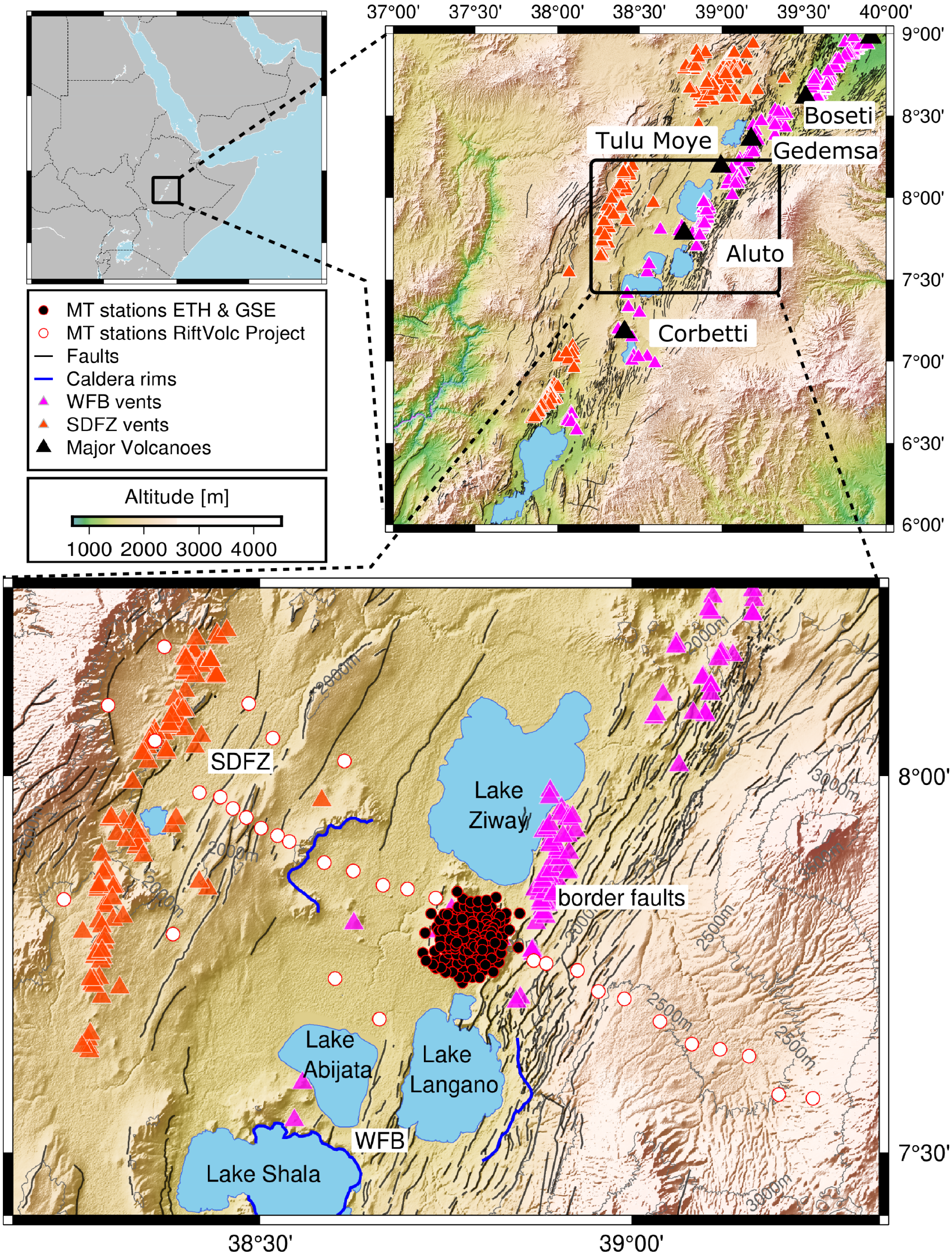

Figure 1. Maps of the study area within East Africa (upper left) and the Main Ethiopian Rift (upper right). The lower map presents the study area in the Central Main Ethiopian Rift with its faults systems (database of faults: Agostini et al., 2011b) and quaternary vents (grouped by Mazzarini & Isola, 2010). The vents belong to two different volcanic belts that are associated with the Wonji Fault Belt (WFB) and the Silti Debre Zeyit Fault Zone (SDFZ). Aluto volcano is located in the center of the study area in between the lakes Ziway and Langano. MT stations are coloured according to the institutions and projects that performed the measurement (MT-dataset by ETH Zurich (ETH) and Geological Survey of Ethiopia (GSE): Samrock et al. (2010) and MT-dataset by the RiftVolc Project: Hübert and Whaler (2020)). The survey area encompasses all fault systems of the CMER (WFB, SDFZ and border faults) and crosses the Gademotta caldera rim west of Aluto. The maximum difference in altitude along the profile is ≈ 1000 m.

value is $\Phi_{max} > 45\,°$ and (iiii) dimensionality of the subsurface with 3-D subsurface features indicated by increased skew-values ($\beta > 3\,°$) (Booker, 2014; Caldwell et al., 2004). A more detailed theoretical background on the phase tensor is provided in the SI (SI: Text S1).

Phase tensor ellipse maps (Fig. 2) indicate that the regional structure of the rift valley is dominated by an increase of electrical conductivity with depth (at $T > 5\,\mathrm{s}$ $\Phi_{max} > 45\,°$). Further, one can observe from ellipticity and skew values that the regional subsurface structure in the western rift valley appears to have stronger lateral contrasts and is more complex (3-D) than in the eastern rift valley. The conductivity structure at Aluto is more complex at shallower depths (e.g. $T = 4.97\,\mathrm{s}$), with relatively stronger lateral conductivity contrasts and 3-D structures in the west and center below the volcanic edifice. These strong local differences of subsurface structure diminish with depth.

We conclude that subsurface electrical conductivity structure is more complex in the western rift area with a strong lateral conductivity contrast, that is approximately oriented either rift-parallel or rift-perpendicular. This $90\,°$-ambiguity is inherent to phase tensor ellipses and inversion of the data is needed to further constrain subsurface conductivity structures. More detailed information on the surveys and the collected MT data is provided in the SI (Text S2).

2.2 3-D Inversion

We used the GoFEM code to perform 3-D forward modelling and inversion (Arndt et al., 2020; A. V. Grayver, 2015; A. V. Grayver & Kolev, 2015). GoFEM uses locally refined meshes to facilitate multi-scale model parameterization (SI: Text S4) and accurately incorporate topography. The code was already used in earlier local-scale MT studies at Aluto (Samrock et al., 2020) and for multi-scale MT studies of volcanically active regions in Mongolia (Käufl et al., 2020).

Since impedance tensors are often affected by galvanic distortions, we first perform a phase tensor inversion. As the starting model for the phase tensor inversion, we used a homogeneous model with a resistivity of $\bar{\rho}^{1D}_{a,ssq} = 19.25\,\Omega\mathrm{m}$, where $\bar{\rho}^{1D}_{a,ssq}$ is the geometric mean of all observed apparent resistivities calculated from Z_{ssq} (SI: Eq. 6-11, see also Rung-Arunwan et al., 2016). We also tested phase tensor inversion runs using different homogeneous starting models with arbitrary higher resistivities ($\rho = 25, 35, 50\,\Omega\mathrm{m}$). The general observation was that starting models with a higher electrical resistivity led to a

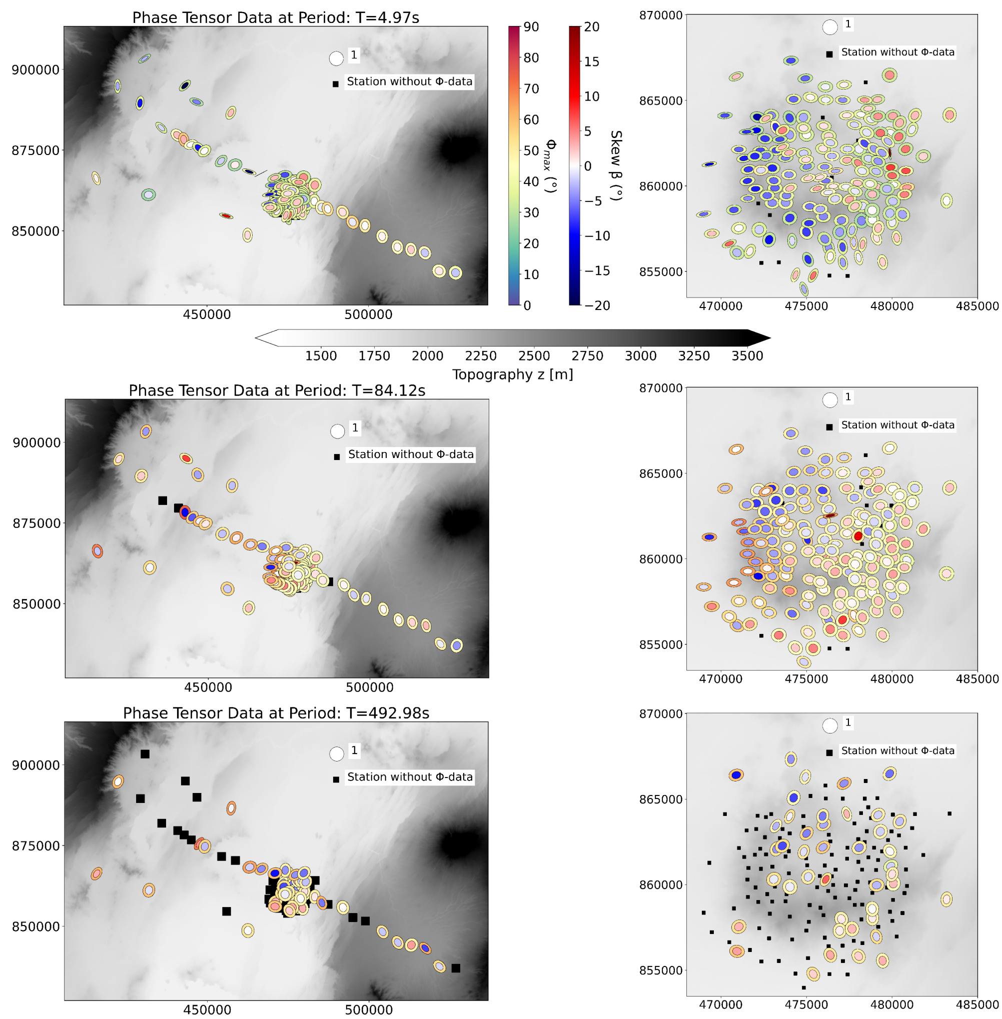

Figure 2. Maps of phase tensor ellipses for different periods at MT stations across the CMER (left) and at Aluto (right) in UTM coordinates. Phase tensor ellipses are normalized by Φ_{max} (see reference ellipse) and coloured by their absolute Φ_{max}-value. The inner core of the ellipses is coloured by the skew (β). Stations that do not have phase tensor data at specific periods due to quality-guided data selection are marked by black squares.

worse convergence and poorer data fit for phase tensor inversion, proving that choosing a data-informed starting model with resistivity ($\bar{\rho}^{1D}_{a,ssq}$) is an adequate choice.

Although phase tensors are free of galvanic distortions (e.g. Caldwell et al., 2004), absolute values of electrical conductivity in models constrained solely by phase tensor data are less constrained, especially when survey layout is sparse (Tietze et al., 2015). To mitigate this limitation, we ran the impedance tensor inversion and used the best-fitting 3-D phase tensor model as a starting model. By doing so, the impedance tensor inversion is guided by the distortion-free phase tensor model and the negative impact of galvanic distortions on the inversion is reduced. If there were no distortions and both phase and impedance tensors contained the same information, we would expect the models to be identical. In reality, the models exhibit some differences, mostly because the impedance tensor inversion need to compensate for galvanic distortions by introducing some scattered conductivity structures at shallow depths (Fig. 2 Samrock et al., 2018) (SI: Fig. S12).

Technical information on the inversion methodology and the achieved data fit for the final phase and impedance tensor models is provided in the SI (Text S3 and S4). In what follows, we will present the final impedance tensor model. The corresponding phase tensor model is shown for completeness in the SI (Text S4.1).

3 Results

Both models, obtained from phase and impedance tensor inversions, fit the observed data within the uncertainty (RMS≤1), given by the error-floor of 5 % applied row-wise to the impedance tensor and propagated to the phase tensor (as in Käufl et al., 2018). Details about the inversion progress and the achieved fit are provided in Fig. 3. Starting at an initial RMS of 2.7, the phase tensor inversion converges to an RMS of 0.83 within four iterations. For the subsequent impedance tensor inversion a relatively low model regularization is chosen, as the large-scale structure is given by the phase tensor model, which is used as the starting model for the impedance tensor inversion. Starting at an initial RMS of 5.1, the impedance tensor inversion converges progressively until a final RMS of 0.81 is achieved (Fig. 3a). The RMS distribution as a function of the period shows that shorter periods tend to yield lower misfits than longer periods (Fig. 3b), which can be due to lower data quality at longer periods. The normalized residuals of both obtained final models are uniformly distributed

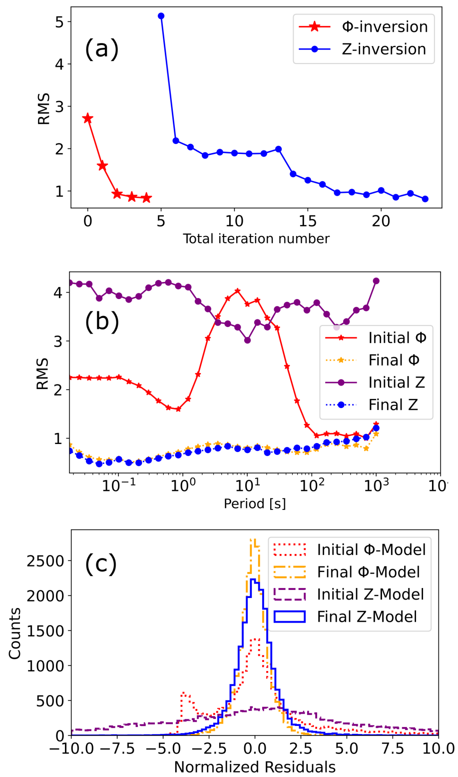

Figure 3. (a) RMS misfit during the phase tensor and the subsequent impedance tensor inversions. (b) RMS misfit versus period for the initial and final phase and impedance tensor inversion runs. (c) Residual distribution of initial and final phase tensor and impedance tensor models. Note that the final phase tensor model is used as a starting model for the impedance tensor inversion.

and centered around zero, indicating that no systematic bias is present (Fig. 3c). More detailed information about the model fit is provided in the SI (Text S5.2).

3.1 Final model

An approximately NW-SE-oriented profile through the final electrical conductivity model is shown in Fig. 4. The presented profile section crosses the entire rift valley and traverses through the center of Aluto volcano. Main electrical conductors (C) in the obtained multi-scale model are described in the following.

The largest conductivity anomaly in the model is the C3 conductor. The maximum recovered electrical conductivity within C3 is $\sigma = 0.18\,\mathrm{S/m}$ (Fig. 4 a). The anomaly occupies a large volume in the lower crust under the western part of the rift and crosses the Moho boundary at depths of $z \approx 30 - 35\,\mathrm{km}$ b.s.l. (Fig. 5). The lateral extent of C3 is about 50 km across the rift and 30 km along the rift, considering the 0.1 S/m isosurface (we note that

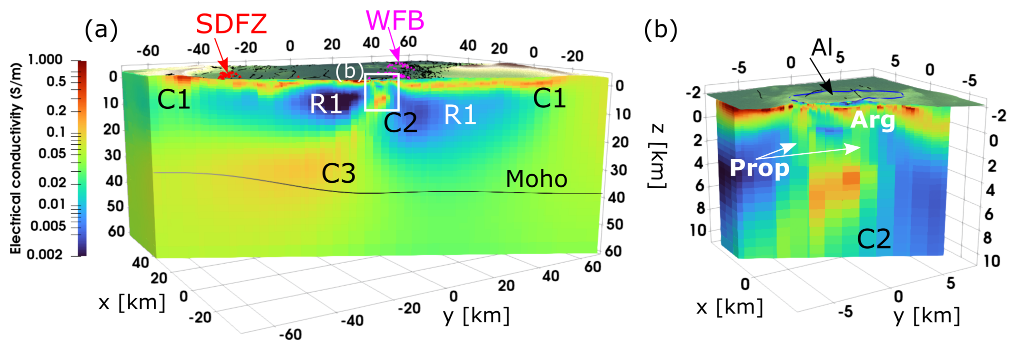

Figure 4. Final 3-D electrical conductivity model. (a) NW-SE oriented cross-section, covering the entire width of the CMER. The Moho boundary (black solid line) is taken from (Stuart et al., 2006). Pink and red triangles depict WFB and SDFZ vents, respectively (see also Fig. 1). Recovered structures are interpreted to be: (C1) Aquifer/sediment unit, (C2) magma ascent channel, (R1) solidified igneous rock and (C3) lower crustal melt ponding zone. The white box marks the area of the Aluto-Langano geothermal system (b). (b) Enlarged excerpt of the Aluto volcano (proposed caldera rim in blue). Increased conductivities in the shallow subsurface can be attributed to a clay cap, formed by argillic alteration (Arg) and higher-temperature propyllitic alteration (Prop).

data coverage along the rift axis is limited). It is evident that no high conductivity zone is found under the eastern part of the rift. C3 ends abruptly around the central rift axis and transitions into a continuously upward propagating channel denoted C2. The C2 structure is characterized by increased bulk electrical conductivities of $\sigma = 1.8\,\mathrm{S/m}$ at depths of $z = 6 - 18\,\mathrm{km}$ b.s.l.. This channel terminates at a depth of $z = 4\,\mathrm{km}$ b.s.l. right below Aluto volcano (Fig. 4 b). At shallower depths (down to about $z \approx 1.5\,\mathrm{km}$ below surface), we recover an electrically conductive layer (C1) that extends across the entire width of the rift, with bulk conductivity values of $\sigma = 0.1 - 0.5\,\mathrm{S/m}$. This continuous layer (C1) is interrupted only under the edifice of Aluto volcano in the center of the shown cross-section (Fig. 4).

A large low-conductivity zone (R1) extends across the valley, with $\sigma \leq 0.01\,\mathrm{S/m}$. R1 is situated in the crust below the continuous conductive layer (C1) and is pierced by the conductive channel C2.

3.2 Interpretation

The presented electrical conductivity model is the first 3-D model of the CMER that images the transcrustal distribution of magma in sufficient detail to interpret it across scales from the lower crust to the surface. In what follows, we provide a geological interpretation of our 3-D electrical conductivity model (Figs. 4, 5 and 6) taking in consideration earlier studies.

3.2.1 C3: Lower crustal magma ponding zone

We interpret this high conductivity anomaly to be caused by the presence of electrically conductive basaltic melt. Hence, C3 represents a zone of melt ponding at the base of the crust. A quantitative melt fraction estimate within C3 is given in Section 3.2.2. The interpretation of C3 as a lower crustal melt ponding zone is supported by seismic observations, geodynamic modelling studies and petrological models for melt evolution and transport in the MER. In the following these studies are presented in more detail.

Volcanic vents above C3 within the western SDFZ tectonic segment are evidence for the presence of a magmatic system in this region (Fig. 1). An indication for the current existence of magma in the area of C3 below the SDFZ is the observed CO_2-degassing in the area (Hunt et al., 2017). That the SDFZ volcanic segment is fed by magma ponding at the base of the crust has also been predicted by several petrological models (e.g. Rooney et al., 2011).

The petrologically constraint models for melt distribution are supported by several geophysical studies. Analysis of seismic S to- P receiver functions has provided evidence for a thinned lithosphere and upwelling asthenosphere below the rift valley of the northern MER. Rychert et al. (2012) performed geodynamic modelling showing that melt generated through decompression melting in the upwelling asthenosphere experiences strong buoyancy forces causing it to migrate into the lower crust, where it accumulates in a melt ponding zone above the Moho.

In the CMER, a similar pronounced low seismic velocity anomaly is observed in the upwelling asthenosphere, which can only be explained by presence of melt that originates from decompression melting (e.g. Chambers et al., 2022; Kim et al., 2012). This melt ponding reservoir is spatially coherent with the C3 structure in our model. It has further been shown that the Moho deepens from west to east in this area (Fig. 4), indicating that asthenospheric upwelling is slightly asymmetric to the rift axis and more pronounced under the western part of the rift (e.g. Keranen & Klemperer, 2008; Stuart et al., 2006).

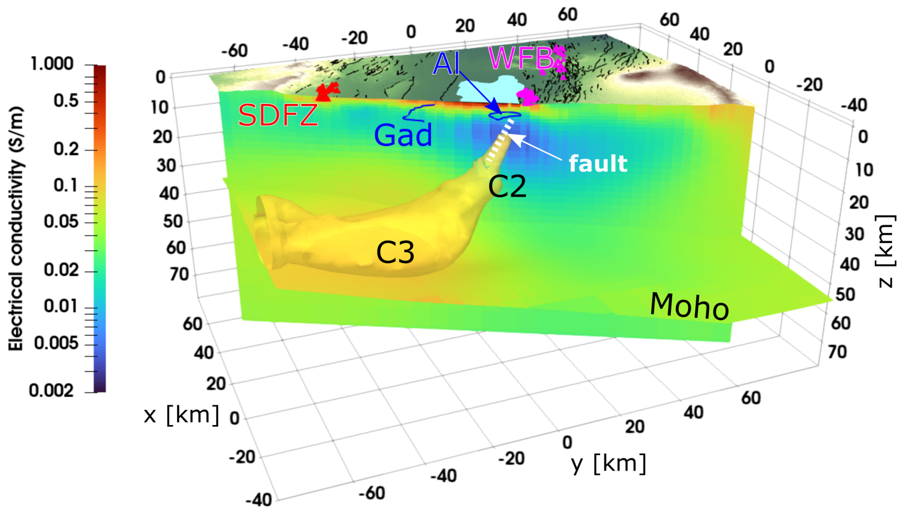

Figure 5. Vertical slice through the final model, approximately along the northern profile line of the MT sites (see Fig. 1). The Moho, as in Fig. 4, is colored by the electrical conductivities at the corresponding depth. The $\sigma = 0.1\,\mathrm{S/m}$-isosurface illustrates the extent of the magmatic ascent channel (C2) and the lower crustal melt ponding zone (C3). The magma ascent channel (C2) is situated exactly beneath Aluto and its dipping angle aligns at shallow depths with the dip angle of the WFB faults (65 °: Corti (2009)). The dipping of faults intersecting Aluto is indicated as a dashed white line. The melt ponding zone (C3) is confined to the area west of the rift-axis and WSW of Aluto volcano. Its lower bound roughly coincides with the Moho. Vents at the WFB and SDFZ are represented as red and pink triangles, respectively. The Gademotta (Gad) caldera rim is shown as a blue line, faults as black lines.

The observation that melt is asymmetrically distributed across the rift has also been made by Hübert et al. (2018), who performed a 2-D inversion of the regional RiftVolc MT dataset used in this study (Fig. 1, see SI: Tab. 1). Further comparison between the models is provided in the discussion (section 4). This asymmetric crustal structure appears comparable to the northern MER, where a regional MT study, approximately 110 km north of our study area imaged high electrical conductivities west of the rift-axis at a depth of about 25 km (Whaler & Hautot, 2006).

Possible reasons for the rift-asymmetry of asthenospheric upwelling and the transcrustal magmatic structure in the general context of different tectonic settings around the world are discussed in Section 4.

Our electrical conductivity model suggests that the melt is not distributed uniformly along the imaged lower crustal segment of the SDFZ, but that melt is focused in a region

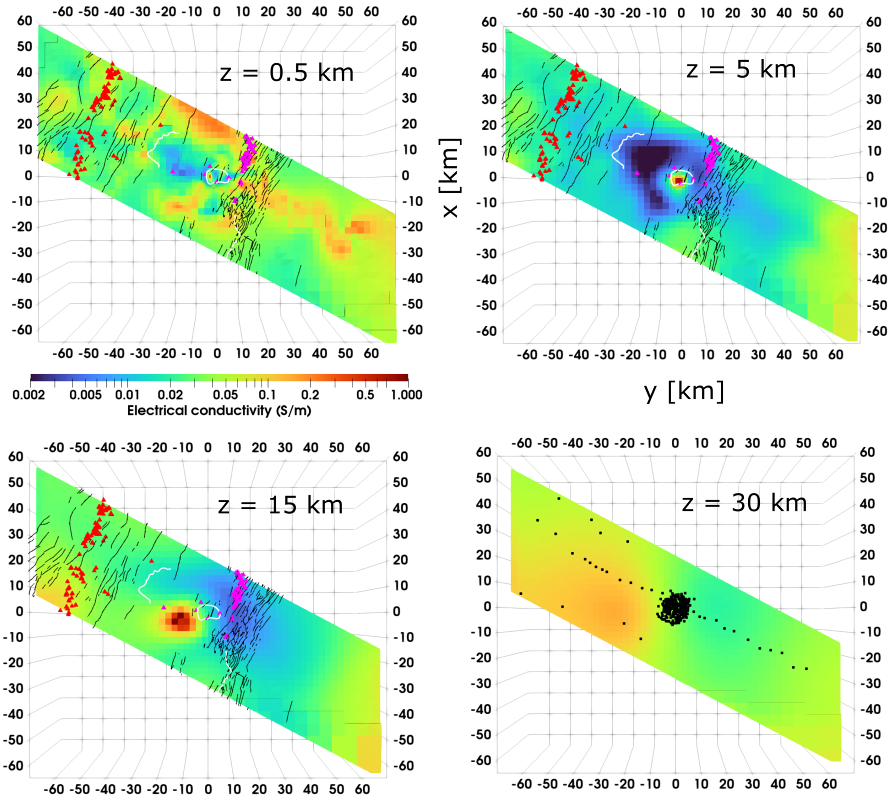

Figure 6. Horizontal slices at several depths from $z = 0.5 - 30\,\mathrm{km}$ b.s.l. through the final impedance tensor model. It is evident from the figure that maximum electrical conductivities occur locally confined to the WSW of Aluto. Pink and red triangles depict WFB and SDFZ vents, respectively, black lines are faults and white lines are the western Gademotta caldera rim and the proposed Aluto caldera rim. Black dots on the 30 km b.s.l. depth slice indicate MT site locations.

spatially confined to the WSW of Aluto (Fig. 5,Fig. 6). To the best of our knowledge, such detailed variations of along-rift melt distributions have not been resolved in the existing regional seismic models (e.g. Chambers et al., 2022; Kim et al., 2012). Our model indicates that lower crustal melt emplacement is much more punctuated and localized than previous geophysical models have shown and than tectonic analogue models have suggested (Corti, 2009, and references therein).

3.2.2 Melt fraction estimates

The model obtained from this study allows us to use electrical conductivity as an independent constraint to quantify the amount of basaltic melt present in the lower crust.

Until now, such estimates in the CMER relied mainly on seismic studies, of which some are summarized in the SI (Tab. S2). Adding electrical conductivity as an additional constraint reduces uncertainty of melt estimates and adds previously lacking knowledge on the spatial extent of the melt reservoir. To estimate the melt content, we used the experiment-calibrated model by Ni et al. (2011) (SI: Text S6), which parameterizes the electrical conductivity of basaltic melt in terms of temperature and dissolved water content. The estimated temperature range for the primary basaltic melt within our interpreted source region (C3) is $\mathcal{T} = 1300 - 1400\,°\mathrm{C}$ (SI: Tab. S2). Thermodynamic modelling of melt evolution constrains the dissolved water content within the parental basaltic melt of samples erupted at Aluto (Gleeson et al., 2017) to $c_{H2O}^{melt} <= 1\,\mathrm{wt\%}$. This amount is well below the maximum water solubility of $c_{H2O}^{melt} = 6.7\,\mathrm{wt\%}$ for identical magma storage conditions, which we calculated using MagmaSat by Ghiorso and Gualda (2015).

Under the relevant conditions (see SI: Tab. S2), the electrical conductivity of a basaltic melt is approximately $\sigma_{melt} = 2.9 - 8.4\,\mathrm{S/m}$ (SI: Fig. S14). Based on the basaltic melt conductivity and the observed range of $\sigma_{bulk} = 0.1 - 0.18\,\mathrm{S/m}$ in the magma ponding zone (C3), we calculate the melt fraction, using a modified Archie's law (SI: Eq. 17 Glover, 2015). The melt fraction is estimated for high melt-connectivities, reflected by a cementation exponent of $m = 1.15$, corresponding to the upper Hashin-Shtrikman bound, and lower connectivities, reflected by $m = 1.5$, which correspond to interstitial melt storage in a matrix of closely packed, perfect spheres (e.g. Glover, 2015). With these constraints, the melt fraction within the C3 conductor is $1.8-7.1$ vol.% and $4.5-14.7$ vol.% for maximum and minimum basaltic melt conductivities, respectively. Seismic studies estimated $2 - 7$ vol.% of vertically aligned melt, based on modelling seismic velocities and seismic anisotropies in the uppermost mantle (J. O. Hammond & Kendall, 2016, SI: Tab. S2), fitting well into the range of our estimates. However, given the estimates from seismic studies, our maximum estimated melt fraction of 14.7 vol.% appears high. It should be noted, that a melt fraction of 14.7 vol.% would be higher than what has been estimated from a MT study in the Afar region (Desissa et al., 2013, SI: Tab. S2). In Afar rifting is far more advanced (Bonini et al., 2005), the crust is thinner (Fig. 3, 4 in Keranen & Klemperer, 2008, and references therein) and in general higher melt fractions than in the CMER are expected in the upper mantle (J. O. Hammond & Kendall, 2016). Hence, we consider the maximum estimate of 14.7 vol.%, and the underlying connectivity model, to be unrealistic, suggesting that higher temperatures, higher water contents and better melt connectivities are the conditions that better describe the in situ setting. In this case, our maximum estimated melt fraction is 7 vol.%. These estimated melt fractions are in agreement with independent estimates that are based on seismic velocities (see SI: Tab. S2) and support the interpretation of the C3 conductor to be a lower crustal magma ponding zone.

3.2.3 C2: Transcrustal magma ascent channel

We interpret the upward rising conductor C2 to be the magma ascent channel in which melt migrates from the deeper melt ponding zone (C3) to the shallow magmatic system beneath Aluto (Fig. 6, 5). The enhanced conductivity within C2 requires that melt is present in the channel up to shallow depths of about 3 km b.s.l.. Hence, the upper part of C2 also represents the magmatic heat source of Aluto's geothermal reservoir (Fig. 4 b). The interpretation of C2 as a mature magmatic ascent channel is supported by petrological studies, which predict that magma under the WFB rises quickly towards the surface, where it either stalls and fractionates to eventually erupt as rhyolite, or the melt erupts quickly as basalt (Mazzarini et al., 2013; Rooney et al., 2011). Another evidence for melt fractions within C2 beneath Aluto is the observed aseismic zone in roughly the same area that was interpreted as hot ductile crust (Wilks et al., 2020). The shallower part of channel C2 has already been described by Samrock et al. (2020, 2021), who noted that the dip of the channel ($\sim 65\,^{\circ}$) is coherent with the dominant fault plane of faults intersecting Aluto volcano. A strong link between magmatic pathways and tectonically weak zones has been described by numerous studies investigating magma-assisted continental rifting (e.g. Casey et al., 2006). The close coupling between active tectonic structures and magma pathways in the CMER is directly observable from the distribution of vents (Fig. 1), which shows that magma preferentially rises along fault zones, where the crust has been weakened (e.g. Mazzarini et al., 2016; Kendall et al., 2005). The spatial conjunction of tectonic and magmatic features further supports the concept of "self-sustained" magmatic segments, where strain is preferentially localized in magmatic segments, which promote intrusions (Beutel et al., 2010; Corti, 2009; Kendall et al., 2005).

3.2.4 R1: Solidified igneous rock

The most striking feature of this electrical resistor is that it is clearly bounded to the west by the Gademotta caldera rim (Fig. 6). The spatial correlation between R1 and the Caldera rim leads us to the most plausible interpretation that R1 constitutes cooled intrusive rock, as has already been previously suggested (Hübert et al., 2018; Samrock et al., 2020). Its formation is likely related to the formation of the Gademotta caldera, where volcanism ceased 1 Ma ago (Hutchison et al., 2016).

3.2.5 C1: Aquifer/sediment unit

In agreement with the conceptual hydrogeological model of the study area by Ghiglieri et al. (2020), the conductor C1 images a shallow layer of pyroclastics and lavas that has been classified as a fissured aquifer. Considering reported groundwater electrical conductivities in the area (Burnside et al., 2021), the most widely distributed observed bulk conductivities within C1 ($\sigma = 0.1 - 0.2\,\mathrm{S/m}$) would require an unreasonably large fluid fraction within C1 (see SI: Text S6.2). It is thus likely that enhanced conductivities in C1 are attributed to a superposition of ionic conduction in porous rocks and sediments as well as electrical conduction through conductive compounds such as clays, which also form through rock weathering processes and are commonly found in soils around the study area (Fritzsche et al., 2007).

3.2.6 Geothermal system

The shallow cap-like conductor ($\sigma = 0.1 - 0.3\,\mathrm{S/m}$), shown in Fig. 4 b under Aluto volcano down to depths of 1.5 km below surface, and the underlying zone of decreased electrical conductivities ($\sigma = 0.02\,\mathrm{S/m}$) between the cap and the upper part of the magma ascent channel C2 are typical features of volcano-hosted, high-temperature geothermal systems (e.g. Bertrand et al., 2012; Omollo et al., 2022; Yamaya et al., 2022). The electrically conductive cap represents the argillic alteration zone, where electrically conductive clays are formed along the flow paths of circulating hot fluids on top of the convective hydrothermal reservoir (e.g. Pellerin et al., 1992). These conductive clay minerals dominate at temperatures of $\mathcal{T} \approx 80 - 220\,^\circ\mathrm{C}$. An electrically more resistive region under the clay cap represents the propylitic alteration zone, where less electrically conductive alteration minerals, such as chlorite and epidote, form at higher temperatures of $\mathcal{T} > 250\,^\circ\mathrm{C}$ (Árnason et al., 2000; Flóvenz et al., 2012; Kristmannsdottir, 1979; Lévy et al., 2018). The C2 structure is the heat source that drives hydrothermal convection (Fig. 4 b). A more detailed description of the geothermal system can be found in previous local MT studies of the Aluto-Langano geothermal field (Cherkose & Mizunaga, 2018; Samrock et al., 2015, 2020).

4 Discussion

The electrical conductivity structure, revealed by our 3-D multi-scale model, is in agreement with the concept and models of magma-assisted continental rifting. A unique feature of our new 3-D model is that it images both the distribution of melt throughout the crust and the geothermal system. Based on this model and previous studies, we present an updated conceptual model of the CMER in Fig. 7 and discuss it below.

Asthenospheric upwelling in the CMER is clearly asymmetric with respect to the rift axis and focused to the western rift valley beneath the SDFZ. The clear focusing of magmatic melt ponding below the SDFZ is surprising, considering that the eastern rift valley is much more active in terms of volcano-tectonic activity along the WFB and eastern border faults (e.g. Corti et al., 2020; Keir et al., 2006; Mazzarini et al., 2013).

A plausible explanation for this asymmetry of asthenospheric upwelling can be an initial inhomogeneity in the lower crust. Modelling has shown, that an area of maximum vertical thickness within a weakened part of the lower crust focuses thinning. Thinning is focused where the crust is thicker, as in this area stronger lithospheric mantle material has been replaced by weaker crust and the deeper Moho is consequently hotter. Hence, an area of initially increased Moho-depth focuses asthenospheric upwelling, decompression melt generation and rifting (e.g. Corti & Manetti, 2006). Such initial crustal inhomogeneities are likely to exist along the MER valley, as it developed within a suture zone of the Mozambique belt, which is a proterozoic continental collision zone (e.g. Fig. 4 in Corti, 2009; Keranen & Klemperer, 2008). However, as magma is not preferentially rising vertically upwards below the SDFZ where the lithosphere is thinnest but moving at an angle towards the eastern WFB (C2) (Fig. 5) one has to assume that other structural controls play a role as well. Two possible mechanisms causing transcrustal magmatic melt migration from the western to the eastern rift valley can be considered: (i) during the early stage of orthogonal rifting lateral squeezing of melt towards border faults (see Fig. 29 in Corti et al., 2003) could have moved magma from the western asthenospheric upwelling zone (C3) to the east (Maccaferri et al., 2014) and (ii) obliquity of the CMER (e.g. Agostini et al., 2011a) leads to extension in the WFB en-échelon structure which facilitates magma supply towards the surface in the WFB during the current rifting stage (Corti, 2009, and references therein).

With respect to magma distribution throughout the crust, the presented multi-scale model reconciles with the concept of transcrustal magmatic mush systems, where magma storage happens at multiple interconnected levels, rather than in isolated voluminous magma chambers (e.g. Cashman et al., 2017; Hill et al., 2022). Indeed, in our model, magma accumulates in the lower crust (C3), where high temperatures maintain melt-hosting regions, even if the magma concentration is low. Segregated magma migrates upwards, below en-échelon systems that weakened the crust, to shallower crustal levels (C2), where melt is stored in a smaller upper crustal reservoir (Fig. 4 b), which represents only a small, uppermost part of a much larger magmatic system (Cashman et al., 2017). Hence the WFB and the magma ascent channel (C2) form a well-developed tectono-magmatic system that allows melt to rise quickly (e.g. Mazzarini et al., 2013; Rooney et al., 2011).

Magmatic melt fractions throughout the crust are estimated to be 7 vol% within the lower crust (C3) and $\sim 10 - 15$ vol% in Aluto's shallow magmatic system (C2) with a magmatic volatile phase of ≥ 5 vol% (Samrock et al., 2021). Hence, the shallow magmatic mush below Aluto is in a highly crystalline degassing state (Samrock et al., 2021) in which it can be considered to be non-eruptible (e.g. Cashman et al., 2017). This study shows that the lower crustal magma ponding zone (C3) can recharge the shallower system with melt and trigger an eruption. However, as the melt fraction in the magma ponding zone is low (7 vol%) no fast significant recharge is to be expected.

In contrast to the crustal structure below the WFB, our model does not show enhanced upper crustal conductivities below the monogenetic vents in the western SDFZ region (Figs. 4,5,6). Such anomalies could have been expected since C3 is the most obvious source of magma for magmatic vents in the SDFZ. The absence of a significant electrical conductivity anomaly under the SDFZ can be explained by the fact that ancient magma channels of the monogenetic vents are ephemeral and cooled quickly. If small amounts of melt are still present, melt is probably stored in the form of a highly crystalline and poorly interconnected mush and is therefore more difficult to image, given the rather sparse distribution of MT stations in this region. This is supported by petrological studies, which suggest that melt rises in a complex dike system and is stored at multiple levels under the SDFZ, where it cools (e.g. Mazzarini et al., 2013; Rooney et al., 2011). The absence of significant amounts of melt in the upper crust under the SDFZ is also in agreement with the observed relatively low seismic activity beneath this area (Keir et al., 2006), which possibly hints at much fewer or no ongoing intrusions in that region. It seems, that the SDFZ accommodates only a subordinate fraction of strain in the CMER, which is consistent with a relatively weak surface expression of faults in the SDFZ compared to the WFB and border

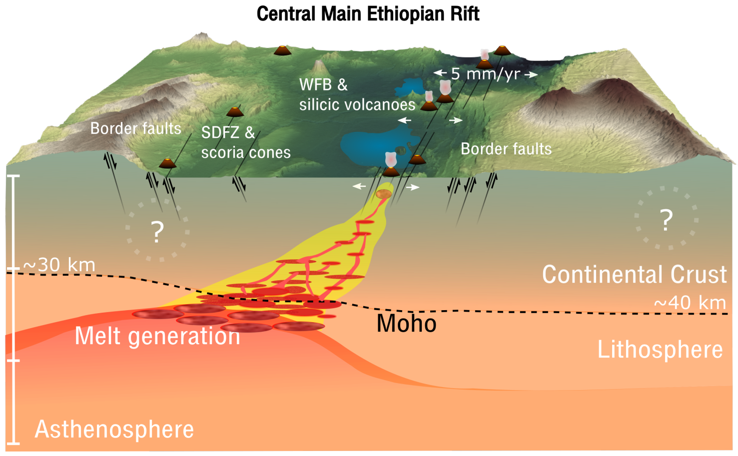

Figure 7. Conceptual model of the CMER. Asthenospheric upwelling leads to decompression melting. Buoyancy effects lead to upward migration of melt and melt ponding in the lower crust. Magma from the lower crustal ponding zone is fed into transcrustal magmatic mush systems that form along structural damage zones. The transcrustal magmatic system below the WFB is well developed. Here, magma rises quickly and fractionates in shallow magma reservoirs beneath silicic volcanoes, such as Aluto. The transcrustal magmatic system below the SDFZ is less mature and is not clearly imaged in this study. This might be caused by a lack of significant amounts of electrically conductive melt below the SDFZ, combined with a sparser MT site spacing in this area. Areas in the conceptual model that are less constrained by data are indicated by a question mark.

faults (Agostini et al., 2011a). The lack of magmatic modification in combination with a relatively low extension activity in the SDFZ support the concept that tectono-magmatic processes in the CMER maintain each other and that the lack of one leads to lower activity of the other (Beutel et al., 2010; Corti, 2009).

However, we note again that the $5-10\,\mathrm{km}$ site spacing in the SDFZ is much larger than at Aluto and smaller-scale variations under the SDFZ might remain undetected in our model. Despite the absence of significant conductivity anomalies in the upper crust under the SDFZ, it is important to point out that volcanic activity in the SDFZ most likely originates from the imaged deeper magmatic ponding zone (C3). Thus, our model suggests that magmas, erupted at the SDFZ and at Aluto within the WFB, may come from a common magma source, which would be the lower crustal magma ponding zone (C3) in our nomenclature. Although some geochemical studies have suggested spatially separated lower crustal melt ponding zones for the volcanoes located along the fault zones of the SDFZ and the WFB (e.g. Rooney et al., 2011), recent studies show that compositional variations can be explained solely by different rates of magma ascent rather than by the existence of distinct melt reservoirs (Nicotra et al., 2021).

Our 3-D model differs in parts from the 2-D model by Hübert et al. (2018), who performed a 2-D inversion of the 120 km long MT profile crossing Aluto (Fig. 1, see SI: Tab. 1). Hübert et al. (2018) imaged a strong conductivity anomaly below the SDFZ, situated at much shallower depths than the lower magma ponding zone (C3) in our model. Furthermore, the 2-D model of Hübert et al. (2018) did not image a magma ascent channel between the deeper source and the Aluto volcano. There can be several reasons for the observed differences between the models. First, a large portion of the data exhibit 3-D effects (see SI: Fig. S4) and, indeed, we observe significant conductivity variations along the rift (Fig. 6), which demand and justify a 3-D modelling approach. Additionally, the density of MT sites in our new study is significantly higher around Aluto, which can further contribute to the observed differences.

To complete the discussion we first put our conceptual model of the CMER (Fig. 7) into the regional context of rifting in the MER and then consider it in a more general context of transcrustal magmatic mush systems throughout different tectonic settings. The CMER as imaged in this study is in an advanced asymmetric rifting stage transitioning between early continental rifiting and incipient continental rupture (e.g. Agostini et al., 2011a). Asymmetric asthenospheric upwelling is considered to be a remnant fingerprint of inherited crustal structures influencing first phases of rifting (Corti & Manetti, 2006) and focused tectono-magmatic activity in the WFB en-échelon structure can be attributed to a more recent second phase rifting stage (e.g. Corti et al., 2003).

A systematic comparison of transcrustal structures throughout the different rifting stages of the MER is difficult since models of the transcrustal magmatic melt distribution comparable to this study are lacking for the northern MER (NMER). However, it is known that the NMER is in a more advanced rifting stage of incipient continental rupture (e.g. Agostini et al., 2011a; Keranen & Klemperer, 2008). The continental crust of the NMER is more symmetric across the rift and thinner than in the CMER (e.g. Stuart et al., 2006). Furthermore, strain is clearly focused in the en-échelon segments (Corti et al., 2018). Hence, the magma-tectonic setting in the NMER suggests that here lower crustal melt ponding is more rift-axis centered and beneath the WFB. This is supported by seismic tomography, which imaged cooled magmatic intrusions directly below the WFB at mid-crustal depth (10 km) (Keranen et al., 2004). However, to the best of our knowledge, the symmetry of the Moho is the only clear indication for more symmetric and probably more rift-centered lower crustal magma ponding in the NMER. Models of rift-wide shear wave velocities, indicative of melting, are not usually detailed enough to reveal significant difference of cross-rift magma distribution at $20-40$ km depth in the CMER and NMER (Fig. 8 in Chambers et al., 2022).

In the context of different tectonic systems worldwide, magmatic underplating and ponding in stacked sills at the base of the crust, as is seen in our model (C3), is a widely adopted concept, but detailed imaging of such zones has been rare (e.g. Cashman et al., 2017; Thybo & Artemieva, 2013). However, there is an increasing number of geophysical MT studies that image such vertically extensive trans-crustal magmatic systems (Bedrosian et al., 2018; Comeau et al., 2016, 2021; Hill et al., 2009, 2022; Käufl et al., 2020; Wannamaker et al., 2008).

A direct comparison of our model from the CMER with the magmatic system volcano Mt. Erebus in the Terror rift of Antarctica imaged by MT reveals similar interdependencies of tectono-magmatic processes. At Mt. Erebus the transcrustal magma distribution has an overall comparable vertically oblique geometry and similar lower crustal melt fractions (10 vol%) comparable to the the CMER (7 vol%) (Hill et al., 2022). However, the two magmatic systems are quite different with respect to their dissolved water content at shallow depth, as CO_2 streaming dehydrates magma at Mt. Erebus (Aluto: H_2O:~ 4.7 wt% (Samrock et al., 2021), Mt. Erebus: H_2O:~ 0.1 wt% (Oppenheimer et al., 2011)). Hill et al. (2022) suggest that the dry magma allows for storage at very shallow depth (≤ 1 km) below Mt. Erebus, which is apparently not the case for Aluto (C2: ≥ 4 km).

The overall transcrustal magma distribution in the CMER, consisting of a broader zone of melt in the lower crust and a magma ascent channel, reconciles also well with subduction arc magmatism (e.g. Comeau et al., 2016; Hill et al., 2009). At Mount St. Helens the estimated lower crustal melt fraction (Hill et al., 2009, 2-12 vol%) is similar to the one of the CMER (7 vol%).

Existing studies throughout different tectonic settings highlighted the significance of the interplay between mantle dynamics and stress and strain distribution within the crust, which controls transcrustal magma distribution. On a global scale processes initiating magmatic supply can be categorized to be either (i) bottom-up controlled through active mantle upwelling and the influence of hot buoyant mantle plumes or (ii) top-down controlled through tectonic processes initiating convection and thus passive magmatic upwelling (e.g. Li et al., 2022). Several 3-D electrical conductivity models so far have imaged lithospheric structures of top-down controlled transcrustal magmatic systems (e.g. Bedrosian et al., 2018; Comeau et al., 2016; Hill et al., 2009; Käufl et al., 2020). However, comparing the results of these studies shows that on a local scale either magmatic or tectonic processes might exercise greater control on the lithosphere. E.g. in a convergent intraplate setting induced asthenospheric upwelling and the subsequent passive magmatism dominate the crustal structure by initiating topographic uplift and volcanism (Comeau et al., 2021; Käufl et al., 2020). In contrast, in subduction systems it has been shown that inhomogeneities in the crust like e.g. variation of lithological units clearly focus magmatism (Bedrosian et al., 2018; Comeau et al., 2016; Hill et al., 2009)), whereas in a ceasing active rifting regime no dominant mechanism could be identified (Wannamaker et al., 2008).

The CMER as imaged in this study is a good example for a system in which both bottom-up and top-down processes did control rifting in the past. It is commonly assumed that rifting in the MER initiated under the influence of a plume (e.g. Corti, 2009, and references therein) (bottom-up control), whereas later asthenospheric upwelling might have been controlled by crustal inhomogeneities (top-down control) (Corti & Manetti, 2006). Today rifting appears to be driven by self-sustaining tectono-magmatic systems, where magma supply and strain focusing enforce each other (Beutel et al., 2010; Corti, 2009).

5 Conclusions and Outlook

Our model provides a 3-D subsurface image of the Aluto volcano region in the MER and reveals regional geological structures across the rift and a local geothermal system under Aluto. The main contributions of this study concern the understanding of rifting processes in the CMER and its tectono-magmatic and geothermal systems, namely: (i) imaging the lower crustal magmatic ponding zone with MT and thereby adding another geophysical constraint (electrical conductivity) to its characterization and (ii) imaging, for the first time, the entire volcano-hydrothermal system under Aluto, along with its connection to the deep-seated lower crustal magma source.

The number of geophysical models imaging transcrustal magmatic mush systems at this scale (e.g. Cashman et al., 2017) is still limited (e.g. Bedrosian et al., 2018; Comeau et al., 2016, 2021; Hill et al., 2009; Huang et al., 2015; Käufl et al., 2020), especially when the setting of actively evolving continental rifts (e.g. Hill et al., 2022; Wannamaker et al., 2008) is considered. Our detailed study provides previously missing geophysical evidence for the hypothesized (e.g. Rooney et al., 2011) conceptual model of the CMER (Fig. 7).

These observations, and the subsequent geological interpretation, were enabled by combining regional and local MT datasets and by using a modern multi-scale magnetotelluric imaging approach. Future regional-scale MT studies along the rift valley are required to provide further insights into along-rift variations of the lower crustal magma ponding zone (C3) and its connection to the volcanic geothermal centers of Tulu Moye and Corbetti, where high-resolution MT surveys, comparable to Aluto, have been conducted (Gíslason et al., 2015; Samrock et al., 2018).

Data availability

The MT data collected at Aluto by ETH Zurich are available from Samrock et al. (2010) via the IRIS EMTF Database: `http://ds.iris.edu/spud/emtf` under the Project entry "Ethiopia", and the survey name "Aluto-Langano Geothermal" . The MT-dataset by project RiftVolc is available from Hübert and Whaler (2020) by DOI: `10.5285/2fb02ed4-5f50-4c14-aeec-27ee13aafc38`. The MT data by the Geological Survey of Ethiopia are available for academic purposes on request from the Geological Survey of Ethiopia, as was the case for this study. The model is available for download in the ETH research collection (`www.research-collection.ethz.ch`) under Dambly et al. (2022) (DOI: `10.3929/ethz-b-000576313`) in form of a Visualization Toolkit (VTK) data file for ParaView.

Declaration of competing interest

The authors declare that they have no known competing financial interests or personal relationships that could have appeared to influence the work reported in this paper.

CReDit Authorship statement

M.L.T.D. performed modelling and inversion of the magnetotelluric data, model visualization and developed numerical tools. F.S. contributed to the 3-D modelling and inversion of the data and model visualization. A.G. developed the GoFEM code and contributed to the 3-D modelling and inversion of the data. All authors interpreted the results and contributed to the writing and review of the paper.

Acknowledgments

M.L.T.D. was supported by ETH Grant ETH-02 19-1. A.G. was supported by the Heisenberg Grant from the German Research Foundation, Deutsche Forschungsgemeinschaft (Project No. 465486300). 3-D inversions and modelling were carried out at the Swiss National Supercomputing Center (CSCS) under project ID s1106. We thank Juliane Hübert and Kathy Whaler from Project RiftVolc and the Geological Survey of Ethiopia for making MT data available. We acknowledge the use of MTPy (Kirkby et al., 2019; Krieger & Peacock, 2014), Generic Mapping Tools (GMT), and Paraview, and thank NASA for providing SRTM digital elevation models. M.O.S., F.S. and M.L.T.D. thank the Werner Siemens Foundation (Werner Siemens-Stiftung) for their endowment of the Geothermal Energy and Geofluids (GEG.ethz.ch) group at ETH Zurich.

References

Agostini, A., Bonini, M., Corti, G., Sani, F., & Manetti, P. (2011a). Distribution of quaternary deformation in the central Main Ethiopian Rift, East Africa. *Tectonics*, *30*(4), 1–21. doi: 10.1029/2010TC002833

Agostini, A., Bonini, M., Corti, G., Sani, F., & Manetti, P. (2011b). *Distribution of quaternary deformation in the central Main Ethiopian Rift, East Africa* [dataset]. (Access Fault Dataset 2.5 `http://ethiopianrift.igg.cnr.it/utilities.htm`) doi: 10.1029/2010TC002833

Árnason, K., Karlsdóttir, R., Eysteinsson, H., Flóvenz, Ó. G., & Gudlaugsson, S. T. (2000). The resistivity structure of high-temperature geothermal systems in Iceland. In *Proceedings of the world geothermal congress 2000* (pp. 923–928). Kyushu-Tohoku, Japan.

Arndt, D., Bangerth, W., Blais, B., Clevenger, T. C., Fehling, M., Grayver, A. V., ... Wells, D. (2020). The deal. II library, version 9.2. *Journal of Numerical Mathematics*, *28*(3), 131–146. doi: 10.1515/jnma-2020-0043

Ayalew, D., Jung, S., Romer, R. L., Kersten, F., Pfänder, J. A., & Garbe-Schönberg, D. (2016). Petrogenesis and origin of modern Ethiopian Rift basalts: Constraints from isotope and trace element geochemistry. *Lithos*, *258-259*, 1–14. doi: 10.1016/j.lithos.2016.04.001

Bedrosian, P. A., Peacock, J. R., Bowles-Martinez, E., Schultz, A., & Hill, G. J. (2018). Crustal inheritance and a top-down control on arc magmatism at Mount St Helens. *Nature Geoscience*, *11*(11), 865–870. doi: 10.1038/s41561-018-0217-2

Benti, N. E., Woldegiyorgis, T. A., Geffe, C. A., Gurmesa, G. S., Chaka, M. D., & Mekonnen, Y. S. (2023). Overview of geothermal resources utilization in Ethiopia: Potentials, opportunities, and challenges. *Scientific African*, e01562. doi: 10.1016/j.sciaf.2023.e01562

Berdichevsky, M. N., & Dmitriev, V. I. (2008). *Models and methods of magnetotellurics.* Springer, Berlin. doi: 10.1007/978-3-540-77814-1

Bertrand, E. A., Caldwell, T. G., Hill, G. J., Wallin, E. L., Bennie, S. L., Cozens, N., ... Wameyo, P. (2012). Magnetotelluric imaging of upper-crustal convection plumes beneath the Taupo Volcanic Zone, New Zealand. *Geophysical Research Letters*, *39*(2). doi: 10.1029/2011GL050177

Beutel, E., van Wijk, J., Ebinger, C., Keir, D., & Agostini, A. (2010). Formation and stability of magmatic segments in the Main Ethiopian and Afar Rifts. *Earth and Planetary Science Letters*, *293*(3-4), 225–235. doi: 10.1016/j.epsl.2010.02.006

Biggs, J., Ayele, A., Fischer, T. P., Fontijn, K., Hutchison, W., Kazimoto, E., ... Wright, T. J. (2021). Volcanic activity and hazard in the East African Rift zone. *Nature Communications*, *12*(1), 1–12. doi: 10.1038/s41467-021-27166-y

Bonini, M., Corti, G., Innocenti, F., Manetti, P., Mazzarini, F., Abebe, T., & Pecskay, Z. (2005, 02). Evolution of the Main Ethiopian Rift in the frame of Afar and Kenya rifts propagation. *Tectonics*, *24*(1). doi: 10.1029/2004TC001680

Booker, J. R. (2014). The magnetotelluric phase tensor: a critical review. *Surveys in Geophysics*, *35*(1), 7–40. doi: 10.1007/s10712-013-9234-2

Buck, W. R. (2004). Consequences of asthenospheric variability on continental rifting. In G. D. Karner, B. Taylor, N. W. Driscoll, & D. L. Kohlstedt (Eds.), *Rheology and deformation of the lithosphere at continental margins* (pp. 1–30). New York: Columbia University Press. doi: 10.7312/karn12738-002

Burnside, N., Montcoudiol, N., Becker, K., & Lewi, E. (2021). Geothermal energy resources in Ethiopia: Status review and insights from hydrochemistry of surface and groundwaters. *Wiley Interdisciplinary Reviews: Water*, e1554. doi: 10.1002/wat2.1554

Caldwell, T. G., Bibby, H. M., & Brown, C. (2004). The magnetotelluric phase tensor. *Geophysical Journal International*, *158*(2), 457–469. doi: 10.1111/j.1365-246X.2004.02281.x

capitalethiopia.com. (2022). *Production tests kick start at Aluto Langano.* Retrieved from `https://www.capitalethiopia.com/capital/production-tests-kick-start-at-aluto-langano/` (accessed 14 October 2022)

Casey, M., Ebinger, C. J., Keir, D., Gloaguen, R., & Mohamed, F. (2006). Strain accommodation in transitional rifts: Extension by magma intrusion and faulting in Ethiopian rift magmatic segments. *Environmental Geochemistry and Health, With Special Reference to Developing Countries*, *259*(2003), 143–163. doi: 10.1144/GSL.SP.2006.259.01.13

Cashman, K. V., Sparks, R. S. J., & Blundy, J. D. (2017). Vertically extensive and unstable magmatic systems: A unified view of igneous processes. *Science*, *355*(6331). doi: 10.1126/science.aag3055

Chambers, E. L., Harmon, N., Keir, D., & Rychert, C. A. (2019). Using ambient noise to image the northern East African Rift. *Geochemistry, Geophysics, Geosystems*, *20*(4), 2091–2109. doi: 10.1029/2018GC008129

Chambers, E. L., Harmon, N., Rychert, C. A., Gallacher, R. J., & Keir, D. (2022, 04). Imaging the seismic velocity structure of the crust and upper mantle in the northern East African Rift using rayleigh wave tomography. *Geophysical Journal International*. doi: 10.1093/gji/ggac156

Chave, A. D., & Jones, A. G. (2012). *The magnetotelluric method: Theory and practice.* Cambridge University Press, New York. doi: 10.1017/CBO9781139020138

Cherkose, B. A., & Mizunaga, H. (2018). Resistivity imaging of Aluto-Langano geothermal field using 3-D magnetotelluric inversion. *Journal of African Earth Sciences*, *139*, 307-318. doi: 10.1016/j.jafrearsci.2017.12.017

Colombier, M., Wadsworth, F. B., Gurioli, L., Scheu, B., Kueppers, U., Di Muro, A., & Dingwell, D. B. (2017, March). The evolution of pore connectivity in volcanic rocks. *Earth and Planetary Science Letters*, *462*(15), 99–109. doi: 10.1016/j.epsl.2017.01.011

Comeau, M. J., Stein, C., Becken, M., & Hansen, U. (2021). Geodynamic modeling of lithospheric removal and surface deformation: Application to intraplate uplift in Central Mongolia. *Journal of Geophysical Research: Solid Earth*, *126*(5), e2020JB021304. doi: 10.1029/2020JB021304

Comeau, M. J., Unsworth, M. J., & Cordell, D. (2016, 10). New constraints on the magma distribution and composition beneath Volcán Uturuncu and the southern Bolivian Altiplano from magnetotelluric data. *Geosphere*, *12*(5), 1391-1421. doi: 10.1130/GES01277.1

Corti, G. (2009). Continental rift evolution: From rift initiation to incipient break-up in the Main Ethiopian Rift, East Africa. *Earth-Science Reviews*, *96*(1-2), 1–53. doi:

10.1016/j.earscirev.2009.06.005

Corti, G., Bonini, M., Conticelli, S., Innocenti, F., Manetti, P., & Sokoutis, D. (2003). Analogue modelling of continental extension: A review focused on the relations between the patterns of deformation and the presence of magma. *Earth-Science Reviews*, *63*(3-4), 169–247. doi: 10.1016/S0012-8252(03)00035-7

Corti, G., & Manetti, P. (2006). Asymmetric rifts due to asymmetric mohos: An experimental approach. *Earth and Planetary Science Letters*, *245*(1), 315-329. doi: 10.1016/j.epsl.2006.02.004

Corti, G., Molin, P., Sembroni, A., Bastow, I. D., & Keir, D. (2018). Control of pre-rift lithospheric structure on the architecture and evolution of continental rifts: Insights from the Main Ethiopian Rift, East Africa. *Tectonics*, *37*(2), 477-496. doi: 10.1002/2017TC004799

Corti, G., Sani, F., Florio, A. A., Greenfield, T., Keir, D., Erbello, A., … Ayele, A. (2020). Tectonics of the Asela-Langano margin, Main Ethiopian Rift (East Africa). *Tectonics*, *39*(8), e2020TC006075. doi: 10.1029/2020TC006075

Dambly, M. L. T., Samrock, F., Grayver, A., & Saar, M. O. (2022). *Transcrustal 3-D electrical conductivity model of the Central Main Ethiopian Rift* [Model]. doi: 10.3929/ethz-b-000576313

Desissa, M., Johnson, N. E., Whaler, K. A., Hautot, S., Fisseha, S., & Dawes, G. J. (2013). A mantle magma reservoir beneath an incipient mid-ocean ridge in Afar, Ethiopia. *Nature Geoscience*, *6*(10), 861–865. doi: 10.1038/ngeo1925

Ebinger, C. (2005, 04). Continental break-up: The East African perspective. *Astronomy & Geophysics*, *46*(2), 2.16-2.21. doi: 10.1111/j.1468-4004.2005.46216.x

Field, L., Blundy, J., Calvert, A., & Yirgu, G. (2013, January). Magmatic history of Dabbahu, a composite volcano in the Afar Rift, Ethiopia. *Bulletin*, *125*(1-2), 128–147. doi: 10.1130/B30560.1

Flóvenz, Ó., Hersir, G., Sæmundsson, K., Ármannsson, H., & Fridriksson, P. (2012). 7.03 - geothermal energy exploration techniques. In A. Sayigh (Ed.), *Comprehensive renewable energy* (p. 51-95). Oxford: Elsevier. doi: 10.1016/B978-0-08-087872-0.00705-8

Fontijn, K., McNamara, K., Tadesse, A. Z., Pyle, D. M., Dessalegn, F., Hutchison, W., … Yirgu, G. (2018). Contrasting styles of post-caldera volcanism along the Main Ethiopian Rift: Implications for contemporary volcanic hazards. *Journal of Volcanology and Geothermal Research*, *356*, 90–113. doi: 10.1016/j.jvolgeores.2018.02.001

Fritzsche, F., Zech, W., & Guggenberger, G. (2007). Soils of the Main Ethiopian Rift valley escarpment: A transect study. *CATENA*, *70*(2), 209-219. doi: 10.1016/j.catena.2006.09.005

Gallacher, R. J., Keir, D., Harmon, N., Stuart, G., Leroy, S., Hammond, J. O., … Ahmed, A. (2016). The initiation of segmented buoyancy-driven melting during continental breakup. *Nature Communications*, *7*, 1–9. doi: 10.1038/ncomms13110

Ghiglieri, G., Pistis, M., Abebe, B., Azagegn, T., Asresahagne Engidasew, T., Pittalis, D., … Haile, T. (2020). Three-dimensional hydrostratigraphical modelling supporting the evaluation of fluoride enrichment in groundwater: Lakes basin (Central Ethiopia). *Journal of Hydrology: Regional Studies*, *32*, 100756. doi: 10.1016/j.ejrh.2020.100756

Ghiorso, M. S., & Gualda, G. A. (2015). An H_2O–CO_2 mixed fluid saturation model compatible with rhyolite-MELTS. *Contributions to Mineralogy and Petrology*, *169*(6), 1–30. doi: 10.1007/s00410-015-1141-8

Gíslason, G., Eysteinsson, H., Björnsson, G., & Hardardóttir, V. (2015). Results of surface exploration in the Corbetti geothermal area, Ethiopia. In *Proceedings world geothermal congress.* Melbourne, Australia.

Gleeson, M. L., Stock, M. J., Pyle, D. M., Mather, T. A., Hutchison, W., Yirgu, G., & Wade, J. (2017). Constraining magma storage conditions at a restless volcano in the Main Ethiopian Rift using phase equilibria models. *Journal of Volcanology and Geothermal Research*, *337*, 44–61. doi: 10.1016/j.jvolgeores.2017.02.026

Glover, P. (2009, January). What is the cementation exponent? A new interpretation. *The Leading Edge*, *28*(1), 82–85. doi: 10.1190/1.3064150

Glover, P. (2015, 04). Geophysical properties of the near surface Earth: Electrical properties. In G. Schubert (Ed.), *Treatise on geophysics* (Second ed., pp. 89–137). Elsevier Oxford. doi: 10.1016/B978-0-444-53802-4.00189-5

Glover, P., Hole, M., & Pous, J. (2000, August). A modified Archie's law for two conducting phases. *Earth and Planetary Science Letters*, *180*(3-4), 369-383. doi: 10.1016/S0012-821X(00)00168-0

Grayver, A., Tietze, K., & Ritter, O. (2013, September). RMS-Rather Meaningless Simplification? In *Proceedings on the 25th schmucker-weidelt-kolloquium für elektromagnetische tiefenforschung* (pp. 31–35). Kirchhundem Rahrbach, Germany.

Grayver, A. V. (2015). Parallel three-dimensional magnetotelluric inversion using adaptive finite-element method. part i: Theory and synthetic study. *Geophysical Journal*

International, *202*(1), 584–603. doi: 10.1093/gji/ggv165

Grayver, A. V., & Kolev, T. V. (2015). Large-scale 3D geoelectromagnetic modeling using parallel adaptive high-order finite element method. *Geophysics*, *80*(6), E277–E291. doi: 10.1190/geo2015-0013.1

Hammond, J. O., & Kendall, J. M. (2016). Constraints on melt distribution from seismology: A case study in Ethiopia. *Environmental Geochemistry and Health, With Special Reference to Developing Countries*, *420*(1), 127–147. doi: 10.1144/SP420.14

Hammond, W. C., & Humphreys, E. D. (2000, May). Upper mantle seismic wave attenuation: Effects of realistic partial melt distribution. *Journal of Geophysical Research, Solid Earth*, *105*(B5), 10987–10999. doi: 10.1029/2000JB900042

Hashin, Z., & Shtrikman, S. (1962). A variational approach to the theory of the elastic behaviour of polycrystals. *Journal of the Mechanics and Physics of Solids*, *10*(4), 343–352. doi: 10.1016/0022-5096(62)90005-4

Hill, G. J., Caldwell, T. G., Heise, W., Chertkoff, D. G., Bibby, H. M., Burgess, M. K., ... Cas, R. A. (2009). Distribution of melt beneath Mount St Helens and Mount Adams inferred from magnetotelluric data. *Nature Geoscience*, *2*(11), 785–789. doi: 10.1038/ngeo661

Hill, G. J., Wannamaker, P. E., Maris, V., Stodt, J. A., Kordy, M., Unsworth, M. J., ... Kyle, P. (2022). Trans-crustal structural control of CO_2-rich extensional magmatic systems revealed at Mount Erebus Antarctica. *Nature Communications*, *13*(1), 1–10. doi: 10.1038/s41467-022-30627-7

Huang, H.-H., Lin, F.-C., Schmandt, B., Farrell, J., Smith, R. B., & Tsai, V. C. (2015). The Yellowstone magmatic system from the mantle plume to the upper crust. *Science*, *348*(6236), 773–776. doi: 10.1126/science.aaa5648

Hübert, J., & Whaler, K. (2020). *Magnetotelluric and transient electromagnetic data from the Main Ethiopian Rift. British Geological Survey. (dataset).* [dataset]. doi: 10.5285/2fb02ed4-5f50-4c14-aeec-27ee13aafc38

Hübert, J., Whaler, K., & Fisseha, S. (2018). The electrical structure of the central Main Ethiopian Rift as imaged by magnetotellurics: Implications for magma storage and pathways. *Journal of Geophysical Research, Solid Earth*, *123*(7), 6019–6032. doi: 10.1029/2017JB015160

Hunt, J. A., Mather, T. A., & Pyle, D. M. (2020). Morphological comparison of distributed volcanic fields in the Main Ethiopian Rift using high-resolution digital elevation models. *Journal of Volcanology and Geothermal Research*, *393*, 106732. doi: 10.1016/j.jvolgeores.2019.106732

Hunt, J. A., Zafu, A., Mather, T. A., Pyle, D. M., & Barry, P. H. (2017). Spatially variable CO_2 degassing in the Main Ethiopian Rift: Implications for magma storage, volatile transport, and rift-related emissions. *Geochemistry, Geophysics, Geosystems*, *18*(10), 3714-3737. doi: 10.1002/2017GC006975

Hutchison, W., Biggs, J., Mather, T. A., Pyle, D. M., Lewi, E., Yirgu, G., ... Fischer, T. P. (2016). Causes of unrest at silicic calderas in the East African Rift: New constraints from InSAR and soil-gas chemistry at Aluto volcano, Ethiopia. *Geochemistry, Geophysics, Geosystems*, *17*(8), 3008–3030. doi: 10.1002/2016GC006395

Iddon, F., & Edmonds, M. (2020). Volatile-rich magmas distributed through the upper crust in the Main Ethiopian Rift. *Geochemistry, Geophysics, Geosystems*, *21*(6). doi: 10.1029/2019GC008904

IRENA. (2020). *Geothermal development in Eastern Africa: Recommendations for power and direct use.* Abu Dhabi: International Renewable Energy Agency.

Jolie, E., Scott, S., Faulds, J., Chambefort, I., Axelsson, G., Gutiérrez-Negrín, L. C., ... Zemedkun, M. T. (2021). Geological controls on geothermal resources for power generation. *Nature Reviews Earth & Environment*, *2*(5), 324–339. doi: 10.1038/s43017-021-00154-y

Kalscheuer, T., Pedersen, L. B., & Siripunvaraporn, W. (2008, November). Radiomagnetotelluric two-dimensional forward and inverse modelling accounting for displacement currents. *Geophysical Journal International*, *175*(2), 486–514. doi: 10.1111/j.1365-246X.2008.03902.x

Käufl, J. S., Grayver, A. V., Comeau, M. J., Kuvshinov, A. V., Becken, M., Kamm, J., ... Demberel, S. (2020). Magnetotelluric multiscale 3-D inversion reveals crustal and upper mantle structure beneath the Hangai and Gobi-Altai region in Mongolia. *Geophysical Journal International*, *221*(2), 1002–1028. doi: 10.1093/gji/ggaa039

Käufl, J. S., Grayver, A. V., & Kuvshinov, A. V. (2018). Topographic distortions of magnetotelluric transfer functions: A high-resolution 3-D modelling study using real elevation data. *Geophysical Journal International*, *215*(3), 1943–1961. doi: 10.1093/gji/ggy375

Keir, D., Ebinger, C. J., Stuart, G. W., Daly, E., & Ayele, A. (2006). Strain accommodation by magmatism and faulting as rifting proceeds to breakup: Seismicity of the northern

Ethiopian Rift. *Journal of Geophysical Research, Solid Earth*, *111*(5), 1–17. doi: 10.1029/2005JB003748

Kelbert, A., Meqbel, N., Egbert, G. D., & Tandon, K. (2014, May). ModEM: A modular system for inversion of electromagnetic geophysical data. *Computers & Geosciences*, *66*, 40–53. doi: 10.1016/j.cageo.2014.01.010

Kendall, J.-M., & Lithgow-Bertelloni, C. (2016). Why is Africa rifting? *Environmental Geochemistry and Health, With Special Reference to Developing Countries*, *420*(1), 11–30. doi: 10.1144/SP420.17

Kendall, J.-M., Stuart, G., Ebinger, C., Bastow, I., & Keir, D. (2005, 01). Magma-assisted rifting in Ethiopia. *Nature*, *433*(7022), 146–148. doi: 10.1038/nature03161

Keranen, K., Klemperer, S., Gloaguen, R., & Group, E. W. (2004, 11). Three-dimensional seismic imaging of a protoridge axis in the Main Ethiopian rift. *Geology*, *32*(11), 949-952. Retrieved from `10.1130/G20737.1` doi: 10.1130/G20737.1

Keranen, K., & Klemperer, S. L. (2008). Discontinuous and diachronous evolution of the Main Ethiopian Rift: Implications for development of continental rifts. *Earth and Planetary Science Letters*, *265*(1-2), 96–111. doi: 10.1016/j.epsl.2007.09.038

Kim, S., Nyblade, A. A., Rhie, J., Baag, C. E., & Kang, T. S. (2012). Crustal S-wave velocity structure of the Main Ethiopian Rift from ambient noise tomography. *Geophysical Journal International*, *191*(2), 865–878. doi: 10.1111/j.1365-246X.2012.05664.x

King, G., & Bailey, G. (2006). Tectonics and human evolution. *Antiquity*, *80*(308), 265–286. doi: 10.1017/S0003598X00093613

Kirkby, A. L., Zhang, F., Peacock, J., Hassan, R., & Duan, J. (2019). The MTPy software package for magnetotelluric data analysis and visualisation. *Journal of Open Source Software*, *4*(37), 1358. doi: 10.21105/joss.01358

Krieger, L., & Peacock, J. R. (2014). MTpy: A python toolbox for magnetotellurics. *Computers & Geosciences*, *72*, 167-175. doi: 10.1016/j.cageo.2014.07.013

Kristmannsdottir, H. (1979). Alteration of basaltic rocks by hydrothermal-activity at 100-300°C. In M. Mortland & V. Farmer (Eds.), *International clay conference 1978* (Vol. 27, p. 359-367). Elsevier. doi: 10.1016/S0070-4571(08)70732-5

Lévy, L., Gibert, B., Sigmundsson, F., Flóvenz, Ó., Hersir, G. P., Briole, P., & Pezard, P. A. (2018). The role of smectites in the electrical conductivity of active hydrothermal systems: Electrical properties of core samples from Krafla volcano, Iceland. *Geophysical Journal International*, *215*(3), 1558–1582. doi: 10.1093/gji/ggy342

Li, S., Li, X., Zhou, J., Cao, H., Liu, L., Liu, Y., ... Jiang, Z. (2022). Passive magmatism on Earth and Earth-like planets. *Geosystems and Geoenvironment*, *1*(1), 100008. doi: 10.1016/j.geogeo.2021.10.003

Maccaferri, F., Rivalta, E., Keir, D., & Acocella, V. (2014). Off-rift volcanism in rift zones determined by crustal unloading. *Nature Geoscience*, *7*(4), 297–300. doi: 10.1038/ngeo2110

Mackenzie, G. D., Thybo, H., & Maguire, P. K. (2005). Crustal velocity structure across the Main Ethiopian Rift: Results from two-dimensional wide-angle seismic modelling. *Geophysical Journal International*, *162*(3), 994–1006. doi: 10.1111/j.1365-246X.2005.02710.x

Mazzarini, F., & Isola, I. (2010). Monogenetic vent self-similar clustering in extending continental crust: Examples from the East African Rift system. *Geosphere*, *6*(5), 567–582. doi: 10.1130/GES00569.1

Mazzarini, F., Le Corvec, N., Isola, I., & Favalli, M. (2016, 06). Volcanic field elongation, vent distribution, and tectonic evolution of a continental rift: The Main Ethiopian Rift example. *Geosphere*, *12*(3), 706-720. doi: 10.1130/GES01193.1

Mazzarini, F., Rooney, T. O., & Isola, I. (2013). The intimate relationship between strain and magmatism: A numerical treatment of clustered monogenetic fields in the Main Ethiopian Rift. *Tectonics*, *32*(1), 49–64. doi: 10.1029/2012TC003146

Mechie, J., Fuchs, K., & Altherr, R. (1994, September). The relationship between seismic velocity, mineral composition and temperature and pressure in the upper mantle—with an application to the Kenya Rift and its eastern flank. *Tectonophysics*, *236*(1-4), 453–464. doi: 10.1016/0040-1951(94)90189-9

Mendelson, K. S., & Cohen, M. H. (1982). The effect of grain anisotropy on the electrical properties of sedimentary rocks. *Geophysics*, *47*(2), 257–263. doi: 10.1190/1.1441332

Ni, H., Keppler, H., & Behrens, H. (2011). Electrical conductivity of hydrous basaltic melts: Implications for partial melting in the upper mantle. *Contributions to Mineralogy and Petrology*, *162*(3), 637–650. doi: 10.1007/s00410-011-0617-4

Nicotra, E., Viccaro, M., Donato, P., Acocella, V., & De Rosa, R. (2021). Catching the Main Ethiopian Rift evolving towards plate divergence. *Scientific Reports*, *11*(1), 1–16. doi: 10.1038/s41598-021-01259-6

Omollo, P., Nishijima, J., Fujimitsu, Y., & Sawayama, K. (2022). Resistivity structural imaging of the Olkaria domes geothermal field in Kenya using 2D and 3D MT data inversion. *Geothermics*, *103*, 102414. doi: 10.1016/j.geothermics.2022.102414

Oppenheimer, C., Moretti, R., Kyle, P. R., Eschenbacher, A., Lowenstern, J. B., Hervig, R. L., & Dunbar, N. W. (2011). Mantle to surface degassing of alkalic magmas at Erebus volcano, Antarctica. *Earth and Planetary Science Letters*, *306*(3), 261-271. doi: 10.1016/j.epsl.2011.04.005

Peccerillo, A., Barberio, M. R., Yirgu, G., Ayalew, D., Barbieri, M., & Wu, T. W. (2003). Relationships between mafic and peralkaline silicic magmatism in continental rift settings: A petrological, geochemical and isotopic study of the Gedemsa volcano, Central Ethiopian Rift. *Journal of Petrology*, *44*(11), 2003–2032. doi: 10.1093/petrology/egg068

Pellerin, L., Johnston, J. M., & Hohmann, G. W. (1992). Evaluation of electromagnetic methods in geothermal exploration. In *Seg technical program expanded abstracts* (Vol. 1, pp. 405–408). Society of Exploration Geophysicists. doi: 10.1190/1.1822102

Ronga, F., Lustrino, M., Marzoli, A., & Melluso, L. (2010). Petrogenesis of a basalt-comendite-pantellerite rock suite: the Boseti Volcanic Complex (Main Ethiopian Rift). *Mineralogy and Petrology*, *98*(1-4), 227–243. doi: 10.1007/s00710-009-0064-3

Rooney, T. O., Bastow, I. D., & Keir, D. (2011). Insights into extensional processes during magma assisted rifting: Evidence from aligned scoria cones. *Journal of Volcanology and Geothermal Research*, *201*(1-4), 83–96. doi: 10.1016/j.jvolgeores.2010.07.019

Rooney, T. O., Furman, T., Yirgu, G., & Ayalew, D. (2005). Structure of the Ethiopian lithosphere: Xenolith evidence in the Main Ethiopian Rift. *Geochimica et Cosmochimica Acta*, *69*(15), 3889–3910. doi: 10.1016/j.gca.2005.03.043

Rooney, T. O., Herzberg, C., & Bastow, I. D. (2012). Elevated mantle temperature beneath East Africa. *Geology*, *40*(1), 27–30. doi: 10.1130/G32382.1

Rung-Arunwan, T., Siripunvaraporn, W., & Utada, H. (2016). On the Berdichevsky average. *Physics of the Earth and Planetary Interiors*, *253*, 1–4. doi: 10.1016/j.pepi.2016.01.006

Rung-Arunwan, T., Siripunvaraporn, W., & Utada, H. (2022, April). The effect of initial and prior models on phase tensor inversion of distorted magnetotelluric data. *Earth, Planets and Space*, *74*(51), 1–24. doi: 10.1186/s40623-022-01611-8

Rychert, C. A., Hammond, J. O., Harmon, N., Michael Kendall, J., Keir, D., Ebinger, C., ... Stuart, G. (2012). Volcanism in the Afar Rift sustained by decompression melting with minimal plume influence. *Nature Geoscience*, *5*(6), 406–409. doi: 10.1038/ngeo1455

Samrock, F., Grayver, A. V., Bachmann, O., Karakas, Ö., & Saar, M. O. (2021). Integrated magnetotelluric and petrological analysis of felsic magma reservoirs: Insights from Ethiopian rift volcanoes. *Earth and Planetary Science Letters*, *559*, 116765. doi: 10.1016/j.epsl.2021.116765

Samrock, F., Grayver, A. V., Cherkose, B., Kuvshinov, A., & Saar, M. O. (2020, 10). Aluto-Langano geothermal field, Ethiopia: Complete image of underlying magmatic-hydrothermal system revealed by revised interpretation of magnetotelluric data. In *Proceedings world geothermal congress (wgc 2020+1)* (p. 11054). Reykjavic, Iceland. doi: 10.3929/ethz-b-000409980

Samrock, F., Grayver, A. V., Eysteinsson, H., & Saar, M. O. (2018). Magnetotelluric image of transcrustal magmatic system beneath the Tulu Moye geothermal prospect in the Ethiopian Rift. *Geophysical Research Letters*, *45*(23), 12–847. doi: 10.1029/2018GL080333

Samrock, F., Kuvshinov, A., Bakker, J., Jackson, A., & Fisseha, S. (2015). 3-D analysis and interpretation of magnetotelluric data from the Aluto-Langano geothermal field, Ethiopia. *Geophysical Journal International*, *202*(3), 1923–1948. doi: 10.1093/gji/ggv270

Samrock, F., Kuvshinov, A., Bakker, J., Jackson, A., Fisseha, S., staff of Addis Ababa University, & the Geological Survey of Ethiopia. (2010). *Magnetotelluric and vertical magnetic transfer functions acquired at the Aluto-Langano geothermal field, Ethiopia* [dataset]. (from the IRIS database, `http://ds.iris.edu/spud/emtf`) doi: 10.17611/DP/EMTF/ETHIOPIA/ETHZ

Schmucker, U., & Weidelt, P. (1975). Electromagnetic induction in the Earth. *Lecture Notes, Aarhus Univ., Denmark.*

Sen, P., Scala, C., & Cohen, M. (1981). A self-similar model for sedimentary rocks with application to the dielectric constant of fused glass beads. *Geophysics*, *46*(5), 781–795. doi: 10.1190/1.1441215

Sruoga, P., Rubinstein, N., & Hinterwimmer, G. (2004, April). Porosity and permeability in volcanic rocks: a case study on the Serie Tobífera, South Patagonia, Argentina. *Journal of Volcanology and Geothermal Research*, *132*(1), 31–43. doi: 10.1016/S0377-0273(03)00419-0

Stuart, G., Bastow, I., & Ebinger, C. (2006). Crustal structure of the northern Main Ethiopian Rift from receiver function studies. *Geological Society, London, Special*

Publications, *259*(1), 253-267. doi: 10.1144/GSL.SP.2006.259.01.20

Thybo, H., & Artemieva, I. (2013). Moho and magmatic underplating in continental lithosphere. *Tectonophysics*, *609*, 605–619. doi: 10.1016/j.tecto.2013.05.032

Tietze, K., Ritter, O., & Egbert, G. D. (2015). 3-d joint inversion of the magnetotelluric phase tensor and vertical magnetic transfer functions. *Geophysical Journal International*, *203*(2), 1128–1148. doi: 10.1093/gji/ggv347

Tyburczy, J. A., & Waff, H. S. (1983, March). Electrical conductivity of molten basalt and andesite to 25 kilobars pressure: Geophysical significance and implications for charge transport and melt structure. *Journal of Geophysical Research, Solid Earth*, *88*(B3), 2413–2430. doi: 10.1029/JB088iB03p02413

Wannamaker, P. E., Hasterok, D. P., Johnston, J. M., Stodt, J. A., Hall, D. B., Sodergren, T. L., ... Unsworth, M. J. (2008). Lithospheric dismemberment and magmatic processes of the Great Basin–Colorado Plateau transition, utah, implied from magnetotellurics. *Geochemistry, Geophysics, Geosystems*, *9*(5). doi: 10.1029/2007GC001886

Weidelt, P. (1972, December). The inverse problem of geomagnetic induction. *Journal of Geophysics*, *38*, 257-289. doi: 10.1093/gji/35.1.379

Whaler, K., & Hautot, S. (2006). The electrical resistivity structure of the crust beneath the northern Main Ethiopian Rift. *Geological Society, London, Special Publications*, *259*(1), 293–305. doi: 10.1144/GSL.SP.2006.259.01.22

Wilks, M., Rawlinson, N., Kendall, J. M., Nowacki, A., Biggs, J., Ayele, A., & Wookey, J. (2020). The coupled magmatic and hydrothermal systems of the restless Aluto Caldera, Ethiopia. *Frontiers in Earth Science*, *8*(October), 1–14. doi: 10.3389/feart.2020.579699

Yamaya, Y., Suzuki, Y., Murata, Y., Okamoto, K., Watanabe, N., Asanuma, H., ... Uchida, T. (2022). 3-D resistivity imaging of the supercritical geothermal system in the Sengan geothermal region, NE Japan. *Geothermics*, *103*, 102412. doi: 10.1016/j.geothermics.2022.102412